Supplement of Atmos. Chem. Phys., 22, 6971–6987, 2022
https://doi.org/10.5194/acp-22-6971-2022-supplement

Supplement of

Reversible and irreversible gas–particle partitioning of dicarbonyl compounds observed in the real atmosphere

Jingcheng Hu et al.

Correspondence to: Zhongming Chen (zmchen@pku.edu.cn)

Temperature dependence of gas-particle partitioning coefficients

Previous studies(Qian et al., 2019; Shen et al., 2018; Cui et al., 2021; Odabasi and Seyfioglu, 2005) have confirmed that high temperature impaired the partitioning of dicarbonyls from gas-phase to particle-phase and a higher uptake coefficient was measured at a lower temperature(Gomez et al., 2015; Zhao et al., 2006). High temperature promote the volatilization and molecular velocities of dicarbonyls causing less dicarbonyls will remain in particles(Xu et al., 2020). What's more, low temperature and high humidity are conducive to hygroscopic aerosols growth and dicarbonyls could easily dissolve into hygroscopic aerosols during their growth(Mitsuishi et al., 2018).

The uncertainties in K_p^t calculation

According to Eq.2, there would be uncertainties in temperature (T), activity coefficient (ζ), vapor pressure(p_L^0), the absorbing fraction of the total particulate matter (f_{om}), and molecular weight of the organic phase (MW_{OM}) to calculate the theoretical partitioning coefficients (K_p^t). The K_p^t values could increase with increasing temperature T, which ranged from 265.53 K to 310.75 K in our observations. We calculate the K_p^t at the two extreme temperature and the ratios $K_{p,\,310.75}^t/K_{p,\,265.53}^t$ are always lower than three for both glyoxal and methylglyoxal. Aerosol phase activity coefficients ζ are a function of the aerosol composition (Jang et al., 1997; Seinfeld et al., 2001) but are thought to modify K_p^t by less than one order of magnitude (Bowman and Melton, 2004). And f_{om} was little changed during our observations and was usually within ~0.3-0.6 in urban Beijing (Huang et al., 2014; Ma et al., 2022). As for MW_{OM}, previous laboratory experiments have shown that the molecular weight of individual constituents in isoprene SOA and 1,3,5-TMB SOA ranges from 100 to 1000 and that the average molecular weight increases with aerosol age due to oligomerization (Kalberer and M., 2004; Dommen et al., 2006). We used a MW_{OM} value of 200 $g\cdot mol^{-1}$, which was used in previous work (Barsanti and Pankow, 2004; Williams et al., 2010; Shen et al., 2018) and increasing MW_{OM} even to 500 $g\cdot mol^{-1}$ would only reduce K_p^t by a factor of 4. Moreover, we calculated the vapor pressure by the extended aerosol inorganic model (E-AIM, http://www.aim.env.uea.ac.uk/aim/ddbst/pcalc_main.php) (Clegg et al., 1998), the results of which were close to those of other methods, such as the SPARC online calculator (Version 3.1) (Hilal et al., 1995; Healy et al., 2008). Overall, the uncertainty associated with the assumptions made to calculate K_p^t could contribute to the uncertainty in K_p^t values. However, as discussed in our study, the discrepancy between field-measured partitioning coefficients and the theoretical ones was more than five orders of magnitude and the uncertainty in the K_p^t calculation would not change the interpretation and conclusions of this work.

The discrepancy between field-measured partitioning coefficients and theoretical ones

The field-measured gas-particle partitioning coefficients K_p^f were approximately 5–7 orders of magnitudes higher than the corresponding theoretical values calculated by Pankow's absorptive model (Eq.1). The influencing factors in Pankow's absorptive model, like the activity coefficient ζ or absorbing fraction f_{om}, could not explain this great difference between the field-measured values and the theoretical ones. The underestimation of gas-particle partitioning coefficients can be attributed to the misidentification of condensed phase species produced in heterogeneous chemical reactions. The discrepancy could be explained by the complex components in aerosol liquid water. Moreover, effective Henry's law coefficients K_H^f were 2-5 orders of magnitudes higher than the theoretical ones. Figure S4 presents the Setschenow plot of dicarbonyls versus aqueous sulfate, nitrate, and ammonia (SNA) concentration in aerosol. The negative salting constant indicated the "salting in" effects, which could result in exponential solubility, for both glyoxal and methylglyoxal in the real atmosphere. Moreover, both K_p^f and K_H^f of dicarbonyls were more than one magnitude higher than the reported laboratory partitioning coefficient values from chamber experiments (Healy et al., 2008; Healy et al., 2009), indicating that the real atmosphere is more favorable for the partitioning of gaseous dicarbonyls to the particle phase. Actual atmospheric environment conditions and complex particle compositions, such as higher ionic strength, could greatly affect the partitioning process and the chemical reactions in the aerosols.

Calculation of theoretical Henry's law coefficient in pure water

$$\frac{d(\ln H)}{d(1/T)}=-\frac{-\Delta_{sol}H}{R} \qquad \text{(S1)}$$

$$H(T)=H^{\Theta}\times\exp\left(\frac{-\Delta_{sol}H}{R}\times\left(\frac{1}{T}-\frac{1}{T^{\Theta}}\right)\right) \qquad \text{(S2)}$$

Where H(T) ($mol\cdot m^{-3}\cdot Pa^{-1}$) is the Henry's law constant of dicarbonyls in pure water at different ambient temperature T(K); H^{Θ}($mol\cdot m^{-3}\cdot Pa^{-1}$) is the Henry's law constant of dicarbonyls in pure water at standard temperature T^{Θ}(298.15K); $\Delta_{sol}H$ (J/mol) is molar enthalpy of dissolution. For glyoxal, H^{Θ} is 4100 $mol\cdot m^{-3}\cdot Pa^{-1}$, $\frac{-\Delta_{sol}H}{R}$ is 7500 K (Ip et al., 2009); and for methylglyoxal, H^{Θ} is 34 $mol\cdot m^{-3}\cdot Pa^{-1}$, $\frac{-\Delta_{sol}H}{R}$ is 7500 K (Betterton and Hoffmann, 1988).

The proposed thermodynamically favored mechanism for the reversible reactions in the aerosols of glyoxal and methylglyoxal

As shown in Fig. S5, upon hydration, a carbonyl group in glyoxal is protonated by H+, and the sp3 oxygen of a hydroxyl group (acting as a nucleophile) in the hydrated glyoxal (A) attacks the protonated carbonyl to form a hemiacetal. The protonation and reaction of two hydrated glyoxals can also occur and form an acetal (D). Hemiacetal and acetal can mutually transform via hydration/dehydration, and both are likely to undergo further dehydration and intramolecular attack on the sp2 carbon, forming five-membered and six-membered dioxane ring dimers (C). Due to the lower barrier to formation, the dioxolane ring dimer (B) is the thermodynamic sink among all monomers and dimers, followed by open dimer species (D). The stable ring structure can react with additional hydrated glyoxal units followed by subsequent ring closure forming higher molecular-weight polymers (E), which is the endpoint of oligomerization due to kinetic barriers (Kua et al., 2008). Glyoxal cannot access the aldol condensation, because its two adjacent terminal aldehyde groups preclude the enol structure from forming (Barsanti and Pankow, 2005).

Other than glyoxal, both hydrate forms (A’ & B’) of methylglyoxal exist in solutions, and the nucleophilic attack at the aldehyde group is more favored compared to the ketone group. The acetal formation mechanism operates similarly for methylglyoxal in an acidic medium, forming stable ring systems. It should be noted that methylglyoxal can undergo aldol condensation due to its methyl ketone function, which is in equilibrium with the enol form by proton shift and tautomerization. The enol form of methylglyoxal with the structure of β-hydroxy ketone is stabilized in an acidic medium through conjugation with the second carbonyl group (Yasmeen et al., 2010) and can react with the hydrated methylglyoxal, resulting in aldol condensation. The product of aldol condensation (D’) is thermodynamically favored overall and can lead to subsequent oligomerization that retains longer hydrocarbon chains. The products of these chains are more stable than those of hemiacetal formation (Krizner et al., 2009).

Mechanism for the reactions of glyoxal and methylglyoxal with OH radicals in the aqueous phase.

As illustrated in Fig. S6, the reaction of both glyoxal and methylglyoxal with OH radicals in the aqueous phase is initiated by H-atom abstraction, followed by the addition of dissolved O_2 and peroxy-radicals formation. For glyoxal, the peroxy-radicals mainly decompose to glyoxylic acid, which then undergo similar OH radical oxidation and ultimately form oxalic acid, while other peroxy-radicals undergo RO_2–RO_2 reactions to form formic acid. Similarly, in the case of methylglyoxal, the peroxy-radicals mainly decompose to pyruvic acids and partly undergo RO_2–RO_2 reactions to form acetic acids. Pyruvic acids could be continuously oxidized to form oxalic acids or mesoxalic acids. The above chemical mechanism was proposed to explain the OH radical oxidation in dilute solutions like fog and cloud water (Lim et al., 2013; Lim et al., 2010) and does not adequately represent the aqueous chemistry in more concentrated solutions like wet aerosol.

Irreversible uptake of glyoxal and methylglyoxal on aerosols

$$\gamma = \frac{d[X]_P/dt}{Z} \qquad \text{(S3)}$$

$$Z = \frac{1}{4} w S_{aw} [X]_g \qquad \text{(S4)}$$

$$w = \sqrt{\frac{8RT}{\pi M_X}} \qquad \text{(S5)}$$

$$S_{aw}=S_a \times f(RH)=S_a \times [1+a(RH/100)^b] \qquad \text{(S6)}$$

$$[X]_P=\int_0^t \frac{d[X]_P}{dt} \qquad \text{(S7)}$$

where γ is the dimensionless irreversible uptake coefficient, which is calculated by field-measured data in this study; X is carbonyl-glyoxal or methylglyoxal; $[X]_p$ is the net uptake of gas-phase dicarbonyl on aerosols (molecules); t is the sampling time; Z is the collision frequency between gas-phase dicarbonyl and the aerosols' surface (molecules·s^{-1}); ω is the average movement rate of gas-phase dicarbonyl (m·s^{-1}); S_{aw} is the surface area of aerosols (m^2); f(RH) is the dimensionless hygroscopic factor; a and b are experience factors (a=8.8, b=9.7) (Liu et al., 2013); $[X]_g$ is the concentration of gas-phase carbonyl (molecules·m^{-3}); M_X is the average molar mass of gas-phase carbonyl (kg·mol^{-1}); R is the ideal gas constant (8.314 Pa·m^3·K^{-1}·mol^{-1}); and T is the actual temperature during the field measurement.

Figure caption

Table S1: Summary of observation periods, sampling numbers, average values of meteorological parameters, concentrations of measured trace gases and $PM_{2.5}$ of five field observations in different seasons.

Table S2: Comparison between K_p^f/K_p^t values (field-measured partitioning coefficients/theoretical partitioning coefficients) in this study and the values published in previous literatures.

Table S3: Summery of reaction parameters of thermodynamically reversible reactions occur in the aerosol phase that are reported in the previous literature.

Table S4: Product distributions of thermodynamically reversible reaction for glyoxal and methylglyoxal in aerosol liquid water in different seasons (%).

Figure S1: Correlations between $PM_{2.5}$ concentrations by weighing Teflon-based samples and those detected by a TEOM 1400A analyzer in the meteorological station.

Figure S2: The chromatogram for the measured carbonyls: (a) chromatogram for the ten measured carbonyls; (b) the specific chromatogram for glyoxal and methylglyoxal.

Figure S3: Diurnal variations of glyoxal in gas-phase (a) and particle-phase (b) in different seasons.

Figure S4: Temperature dependence of K_p^f for glyoxal (a) and methylglyoxal (b).

Figure S5: Setschenow plot for glyoxal and methylglyoxal with sulfate (a), nitrate (b) and ammonia (c), assuming unit density for pure water.

Figure S6: The proposed thermodynamically favored mechanism of glyoxal and methylglyoxal in the reversible reactions. The dark and blue characters indicated the glyoxal and methylglyoxal, respectively.

Figure S7: Mechanism for the reactions of glyoxal and methylglyoxal with OH radicals in the aqueous phase. The black characters represent dominant pathways, while the blue characters represent minor pathways.

Figure S8: The dependence of aerosol liquid water contents (ALWC) on the relative humidity (RH) with different SNA (sulfate, nitrate and ammonia) concentrations.

Figure S9: Gas-particle partitioning process via irreversible uptake as a function of aerosol composition in different RH conditions.

Figure S10: The correlation-ship between oxalate concentrations measured by IC and those calculated by modeling coupled with full kinetic of glyoxal/methylglyoxal + OH.

Reference

Barsanti, K. C. and Pankow, J. F.: Thermodynamics of the formation of atmospheric organic particulate matter by accretion reactions—2. Dialdehydes, methylglyoxal, and diketones, Atmospheric Environment, 39, 6597-6607, 10.1016/j.atmosenv.2005.07.056, 2005.

Betterton, E. A. and Hoffmann, M. R.: Kinetics, mechanism and thermodynamics of the reversible reaction of methylglyoxal (CH3COCHO) with sulfur(IV), The Journal of Physical Chemistry, 91, 3011-3020, 1987.

Cui, J., Sun, M., Wang, L., Guo, J., Xie, G., Zhang, J., and Zhang, R.: Gas-particle partitioning of carbonyls and its influencing factors in the urban atmosphere of Zhengzhou, China, Science of the Total Environment, 751, 142027, 10.1016/j.scitotenv.2020.142027, 2021.

Fratzke, A. R. and Reilly, P. J.: Thermodynamic and kinetic analysis of the dimerization of aqueous glyoxal, International Journal of Chemical Kinetics, 18, 775–789, 1986.

Gomez, M. E., Lin, Y., Guo, S., and Zhang, R.: Heterogeneous chemistry of glyoxal on acidic solutions. An oligomerization pathway for secondary organic aerosol formation, J Phys Chem A, 119, 4457-4463, 10.1021/jp509916r, 2015.

Jang and M.: Heterogeneous atmospheric aerosol production by acid-catalyzed particle-phase reactions, Science, 298, 814-817, 2002.

Jessen, C. Q., Kollerup, F., Nielsen, K., Ovesen, H., and Sørensen, P.: The Hydration of Glyoxal and Methylglyoxal in Aqueous Solution, Bulletin des Societes Chimiques Belges, 91, 396-396, 1982.

Krizner, H. E., Haan, D. D., and Kua, J.: Thermodynamics and kinetics of methylglyoxal dimer formation: a computational study, Journal of Physical Chemistry A, 113, 6994-7001, 2009.

Kua, J., Hanley, S. W., and Haan, D. D.: Thermodynamics and Kinetics of Glyoxal Dimer Formation: A Computational Study, The Journal of Physical Chemistry A, 112, 66-72, 2008.

Lim, Y. B., Tan, Y., and Turpin, B. J.: Chemical insights, explicit chemistry, and yields of secondary organic aerosol from OH radical oxidation of methylglyoxal and glyoxal in the aqueous phase, Atmospheric Chemistry and Physics, 13, 8651-8667, 10.5194/acp-13-8651-2013, 2013.

Lim, Y. B., Tan, Y., Perri, M. J., Seitzinger, S. P., and Turpin, B. J.: Aqueous chemistry and its role in secondary organic aerosol (SOA) formation, Atmospheric Chemistry and Physics, 10, 10521-10539, 10.5194/acp-10-10521-2010, 2010.

Liu, X., Gu, J., Li, Y., Cheng, Y., Yu, Q., Han, T., Wang, J., Tian, H., Jing, C., and Zhang, Y.: Increase of aerosol scattering by hygroscopic growth: Observation, modeling, and implications on visibility, Atmospheric Research, 132-133, 91-101, 2013.

Mitsuishi, K., Iwasaki, M., Takeuchi, M., Okochi, H., Kato, S., Ohira, S.-I., and Toda, K.: Diurnal Variations in Partitioning of Atmospheric Glyoxal and Methylglyoxal between Gas and Particles at the Ground Level and in the Free Troposphere, ACS Earth and Space Chemistry, 2, 915-924, 10.1021/acsearthspacechem.8b00037, 2018.

Odabasi, M. and Seyfioglu, R.: Phase partitioning of atmospheric formaldehyde in a suburban atmosphere, Atmospheric Environment, 39, 5149-5156, 10.1016/j.atmosenv.2005.05.006, 2005.

Qian, X., Shen, H., and Chen, Z.: Characterizing summer and winter carbonyl compounds in Beijing atmosphere, Atmospheric Environment, 214, 10.1016/j.atmosenv.2019.116845, 2019.

Shen, H., Chen, Z., Li, H., Qian, X., Qin, X., and Shi, W.: Gas-Particle Partitioning of Carbonyl Compounds in the Ambient Atmosphere, Environmental Science & Technology, 52, 10997-11006, 10.1021/acs.est.8b01882, 2018.

Xu, R., Li, X., Dong, H., Wu, Z., Chen, S., Fang, X., Gao, J., Guo, S., Hu, M., Li, D., Liu, Y., Liu, Y., Lou, S., Lu, K., Meng, X., Wang, H., Zeng, L., Zong, T., Hu, J., Chen, M., Shao, M., and Zhang, Y.: Measurement of gaseous and particulate formaldehyde in the Yangtze River Delta, China, Atmospheric Environment, 224, 10.1016/j.atmosenv.2019.117114, 2020.

Yasmeen, F., Sauret, N., Gal, J. F., Maria, P. C., Massi, L., Maenhaut, W., and Claeys, M.: Characterization of oligomers from methylglyoxal under dark conditions: a pathway to produce secondary organic aerosol through cloud processing during nighttime, Atmospheric Chemistry and Physics, 10, 2010.

Zhao, J., Levitt, N. P., Zhang, R., and Chen, J.: Heterogeneous reactions of methylglyoxal in acidic media: implications for secondary organic aerosol formation, Environmental Science & Technology, 40, 7682-7687, 2006.

Table S1: Summary of observation periods, sampling numbers, average values of meteorological parameters, concentrations of measured trace gases and $PM_{2.5}$ of five field observations in different seasons.

	summer	spring	autumn	winter	
periods	2019.07.20-08.04	2021.03.26-04.06	2020.10.24-11.07	2020.01.05-01.19	2021.01.08-01.26
gas-phase	77	52	79	83	96
particle-phase	25	19	26	28	32
CO (ppmv)	0.54	0.46	0.50	0.73	0.69
NO (ppbv)	1.13	4.43	20.65	15.62	9.12
NO_2 (ppbv)	14.24	15.89	14.67	22.50	16.94
SO_2 (ppbv)	0.096	1.36	2.26	2.98	2.53
O_3 (ppbv)	70.99	36.10	19.55	15.44	19.02
$PM_{2.5}$ (μg/m^3)	58.40	76.93	52.61	45.04	56.00
T (K)	301.14	289.44	287.20	273.85	273.48
RH (%)	67.41	29.66	23.99	31.03	30.16
WS (m/s)	1.93	2.83	2.55	2.21	2.78

Table S2: Comparison between K_p^f/K_p^t values (field-measured partitioning coefficients/theoretical partitioning coefficients) in this study and the values published in previous literatures.

Dicarbonyls	Seasons	K_p^f	K_p^f/K_p^t	Reference
Glyoxal	summer	3.23×10^{-4}	8.90×10^{5}	Qian et al. (2019)
		6.31×10^{-4}	1.32×10^{6}	Cui et al. (2021)
		1.02×10^{-1}	/	Ortiz et al. (2013)
		8.11×10^{-4}	2.48×10^{6}	This study
	winter	1.44×10^{-3}	1.13×10^{6}	Shen et al. (2018)
		1.71×10^{-3}	1.05×10^{6}	Cui et al. (2021)
		1.30×10^{-2}	1.02×10^{7}	This study
	spring	1.33×10^{-3}	1.80×10^{6}	Cui et al. (2021)
		1.43×10^{-2}	3.55×10^{7}	This study
	autumn	1.05×10^{-3}	1.26×10^{6}	Cui et al. (2021)
		2.14×10^{-3}	3.41×10^{6}	This study
Methylglyoxal	summer	4.07×10^{-5}	5.22×10^{4}	Qian et al. (2019)
		1.40×10^{-4}	1.31×10^{5}	Cui et al. (2021)
		7.41×10^{-2}	/	Ortiz et al. (2013)
		1.49×10^{-4}	2.10×10^{5}	This study
	winter	4.19×10^{-4}	1.53×10^{5}	Shen et al. (2018)
		4.27×10^{-4}	1.16×10^{5}	Cui et al. (2021)
		2.60×10^{-3}	9.93×10^{5}	This study
	spring	3.48×10^{-4}	2.10×10^{5}	Cui et al. (2021)
		1.06×10^{-3}	8.77×10^{5}	This study
	autumn	2.07×10^{-4}	1.11×10^{5}	Cui et al. (2021)
		9.55×10^{-4}	7.07×10^{5}	This study

Table S3: Summery of reaction parameters of thermodynamically reversible reactions occur in the aerosol phase that are reported in the previous literature.

Dicarbonyl	Reaction	Equilibrium constant	Rate constant forward k/backward k’	Reference
Glyoxal	Hydration			Wasa and Musha, 1970
	Hydr1	350	$k=7\ s^{-1}$; $k'=0.02\ s^{-1}$	Betterton and Hoffmann, 1988
	Hydr2	207	$k=4\ s^{-1}$; $k'=0.02\ s^{-1}$	Ip et al., 2009
	Dimerization	$0.56\ M^{-1}$	$k=10^{-4}\ M^{-1}\cdot s^{-1}$; $k'=1.8\times10^{-4}\ M^{-1}\cdot s^{-1}$	Fratzke and Reilly,1986
	Trimerization	1000	$k=100\ M^{-1}\cdot zzs^{-1}$; $k'=0.1\ M^{-1}\cdot s^{-1}$	Volkamer, 2009 Volkamer, 2010
Methylglyoxal	Hydration			Jessen, 1982
	Hydr1	2700	$k=35\ s^{-1}$; $k'=0.013\ s^{-1}$	Betterton and Hoffmann, 1987
	Hydr2	0.24	$k=0.0048\ s^{-1}$; $k'=0.02\ s^{-1}$	Matthew J. Elrod, 2021
	Polymerization	1000	$k=100\ M^{-1}\cdot s^{-1}$; $k'=0.1\ M^{-1}\cdot s^{-1}$	The same as glyoxal

Table S4: Product distributions of thermodynamically reversible formation for glyoxal and methylglyoxal in aerosol liquid water in different seasons (%).

Season	Glyoxal		Methylglyoxal	
	Hydrates	Oligomers	Hydrates	Oligomers
Summer	52.80	47.30	35.10	64.98
Autumn	19.00	79.75	20.30	77.35
Spring	14.64	85.43	21.03	78.97
Winter	13.92	86.15	18.78	86.31
General	16.3	83.5	20.8	80.8

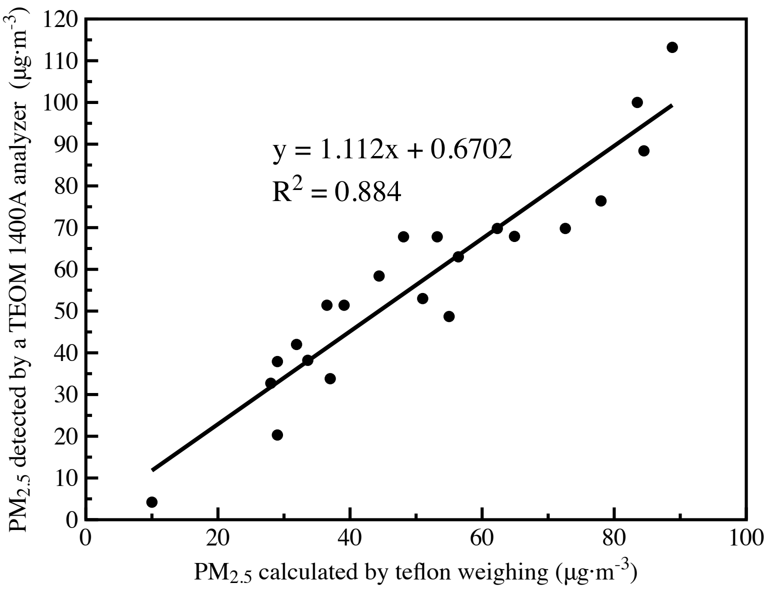

Figure S1: Correlations between $PM_{2.5}$ concentrations by weighing Teflon-based samples and those detected by a TEOM 1400A analyzer in the meteorological station.

(a) Chromatogram for standard solution of ten carbonyls

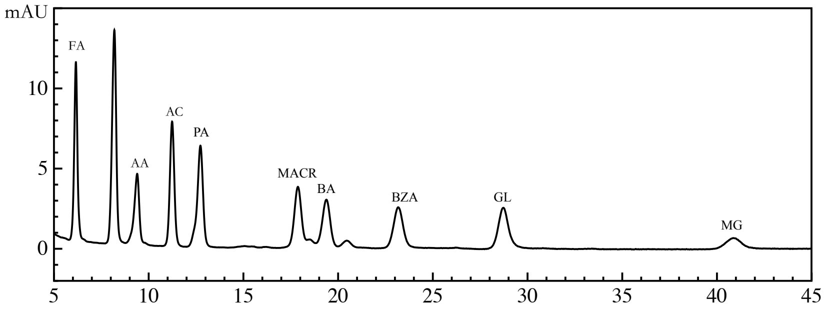

(b) Chromatogram for standard solution of glyoxal and methylglyoxal

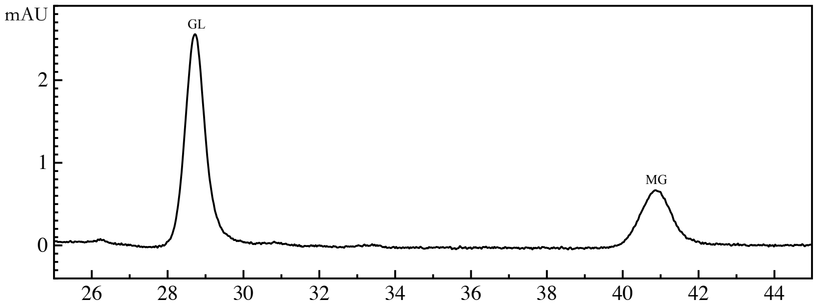

(c) Chromatogram for extraction of sampling filters

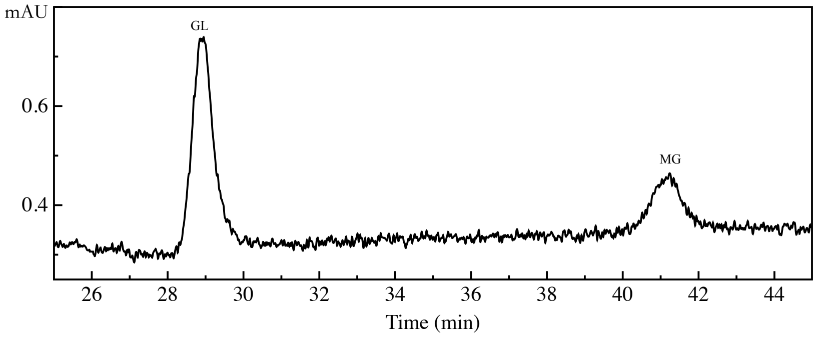

Figure S2: The chromatogram for the measured carbonyls. (a) chromatogram for standard solutions of ten measured carbonyls; (b) specific chromatogram for standard solutions of glyoxal and methylglyoxal; (c) chromatogram for extraction of sampling filters (FA: formaldehyde; AA: acetaldehyde; AC: acetone; PA: propionaldehyde; MACR: methacrolein; BA: butyraldehyde; MVK: methyl vinyl ketone; BZA: benzaldehyde; GL: glyoxal; MG: methylglyoxal).

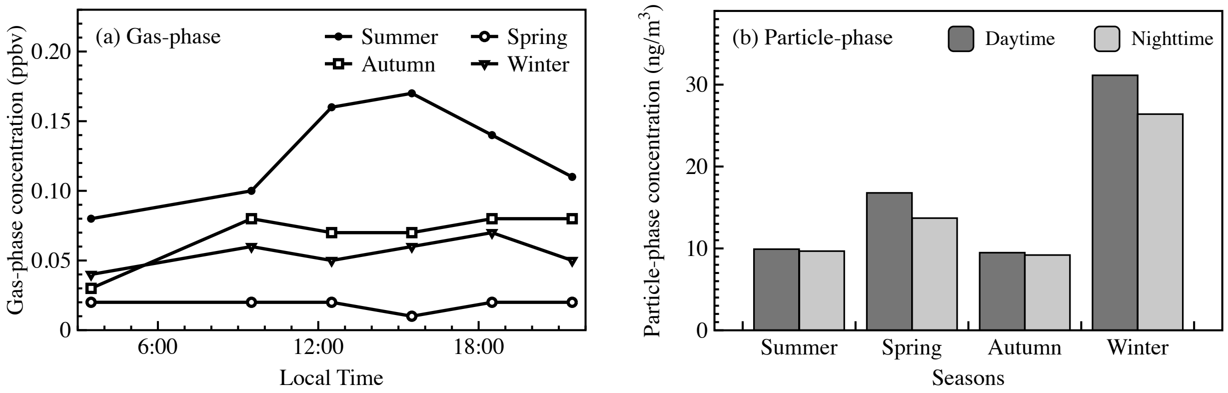

Figure S3: Diurnal variations of glyoxal in gas-phase (a) and particle-phase (b) in different seasons.

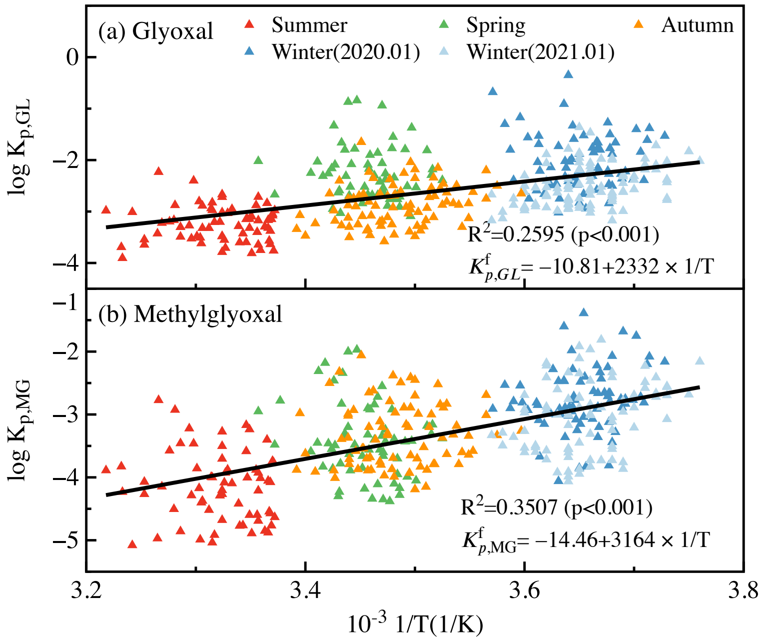

Figure S4: Temperature dependence of K_p^f for glyoxal (a) and methylglyoxal (b). Colors represent different seasons.

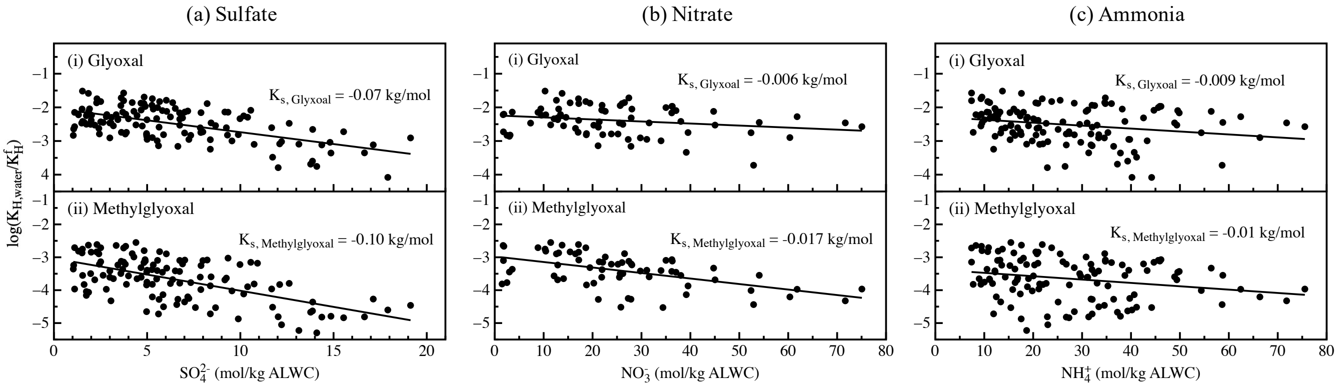

Figure S5: Setschenow plot for glyoxal and methylglyoxal with sulfate (a), nitrate (b) and ammonia (c), assuming unit density for pure water.

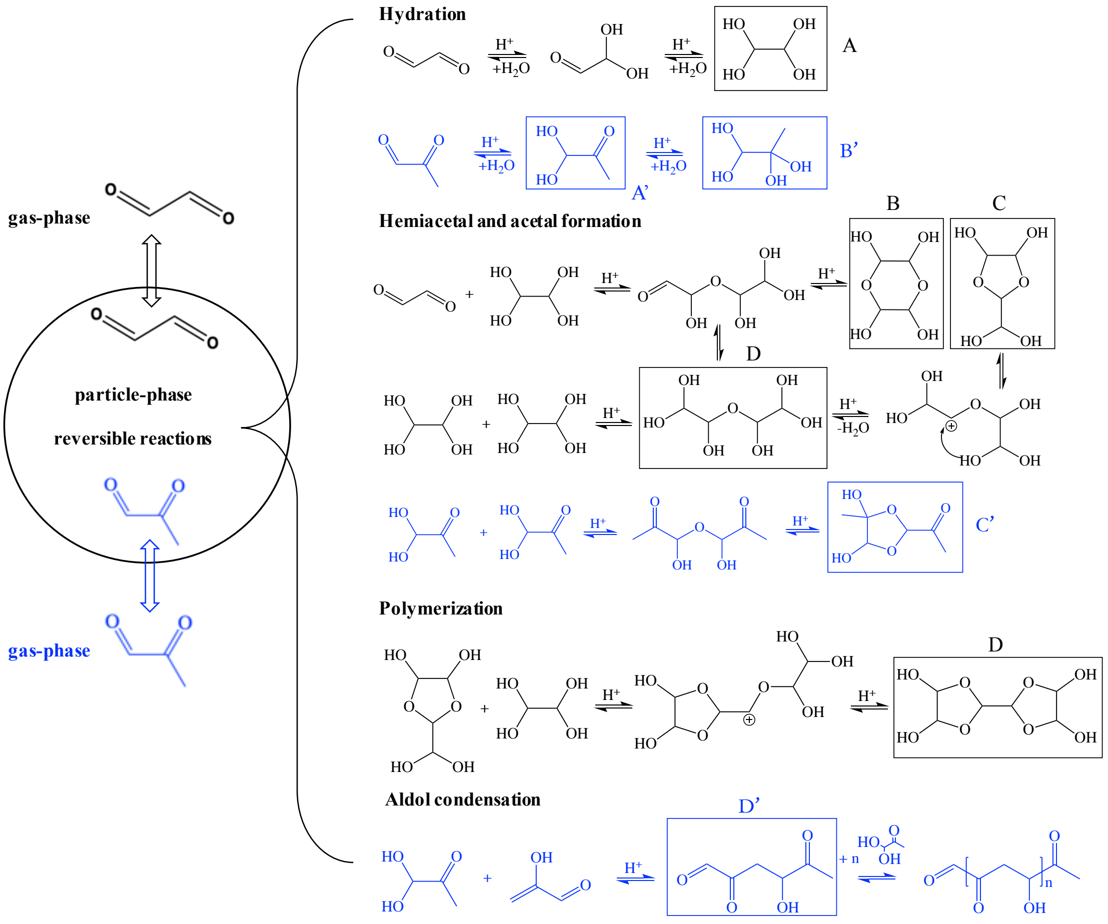

Figure S6: The proposed thermodynamically favored mechanism of glyoxal and methylglyoxal in the reversible reactions. The dark and blue characters indicated the glyoxal and methylglyoxal, respectively. The figure was referenced from Jang and M. (2002)

Glyoxal + OH mechanisms

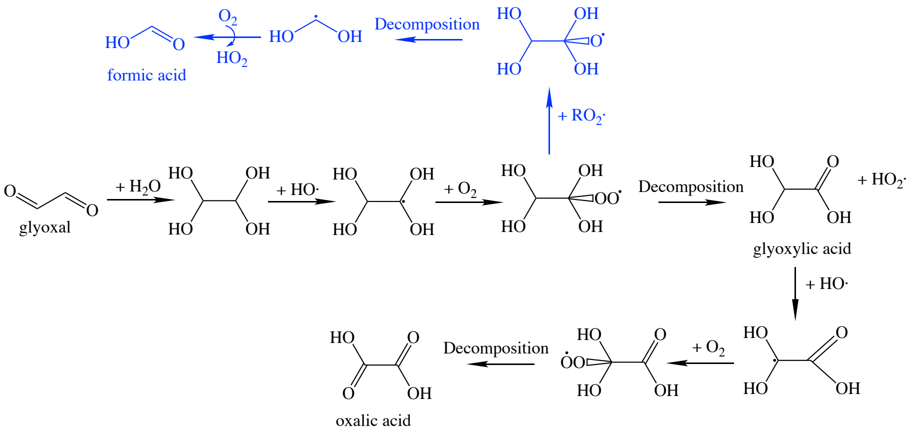

Methylglyoxal + OH mechanisms

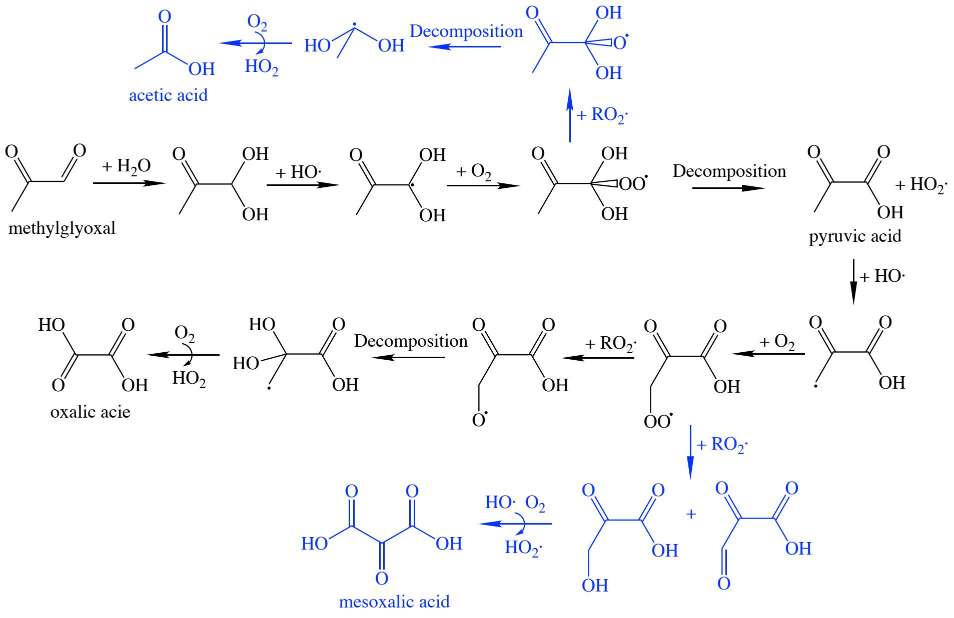

Figure S7: Mechanism for the reactions of glyoxal and methylglyoxal with OH radicals in the aqueous phase. The black characters represent dominant pathways, while the blue characters represent minor pathways.

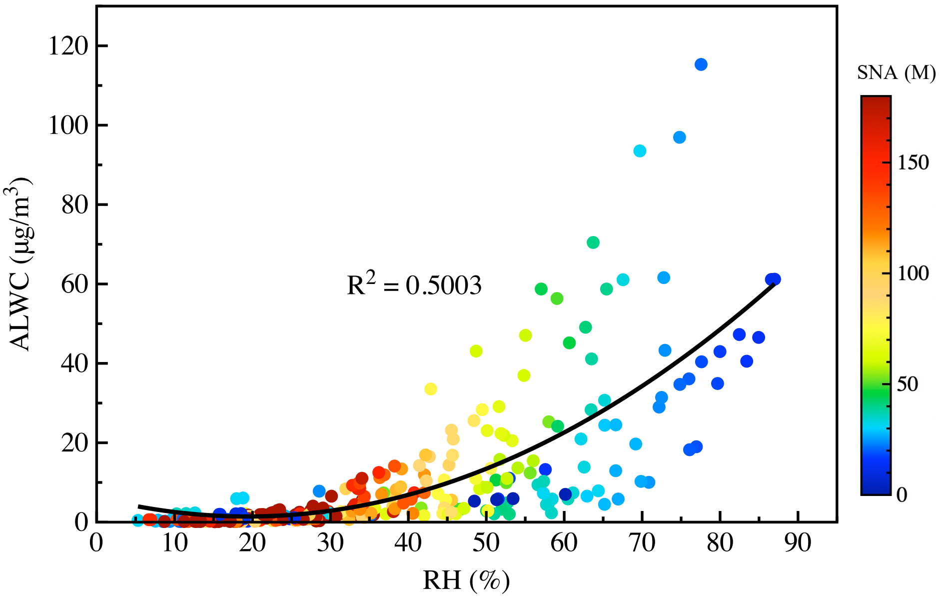

Figure S8: The dependence of aerosol liquid water contents (ALWC) on the relative humidity (RH) with different SNA (sulfate, nitrate and ammonia) concentrations.

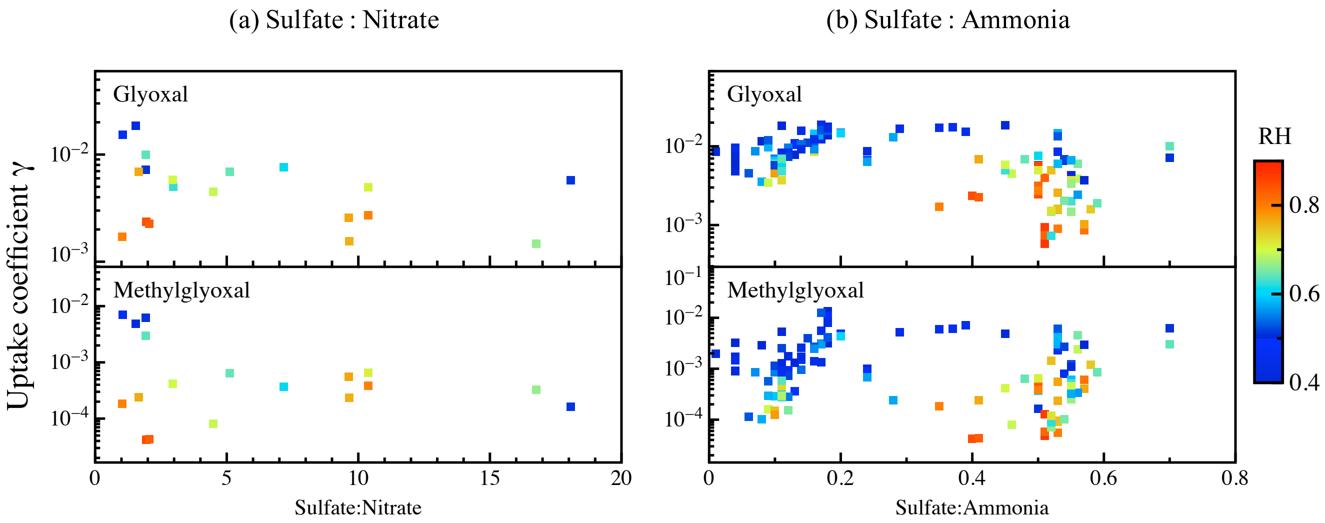

Figure S9: Gas-particle partitioning process via irreversible uptake as a function of aerosol composition in different RH conditions, the concentration unit for SNA in the ratios is molality (mol/L ALWC).

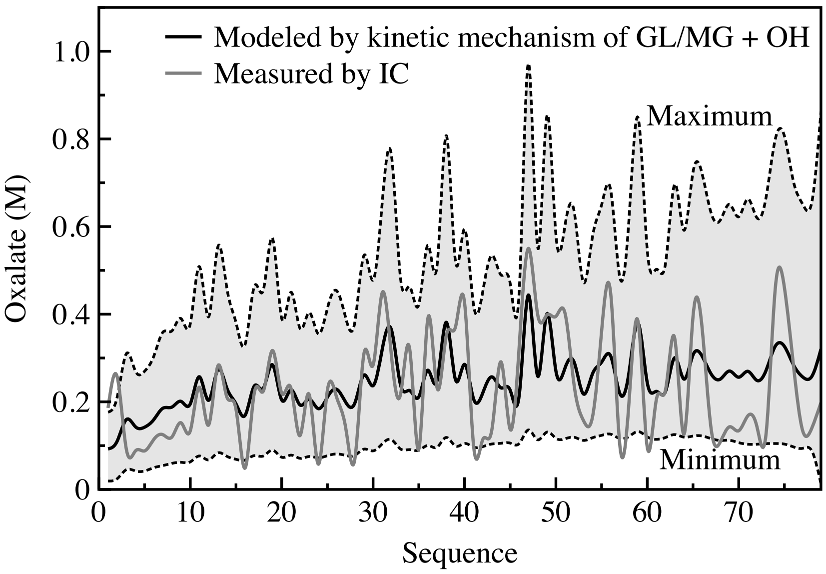

Figure S10: The correlation between oxalate concentrations measured by ion chromatography (gray lines) and those calculated by modeling coupled with the full kinetic of glyoxal/methylglyoxal + OH (black lines). The sequence number refers to the serial number of samples. And the grey shaded area refers to the variation range of modeled oxalate concentrations, which is constrained by OH concentrations in aerosol liquid water.